Annals of Glaciology

Article

Cite this article: Traversa G, Scipinotti R, Pierattini S, Bianchi Fasani G, Di Mauro B (2024). Cryoconite holes geomorphometry, spatial distribution and radiative impact over the Hells Gate Ice Shelf, East Antarctica. *Annals of Glaciology* 1–10. https://doi.org/10.1017/aog.2024.20

Received: 29 December 2023
Revised: 25 March 2024
Accepted: 9 April 2024

Keywords:
Antarctic glaciology; blue ice; ice shelves; remote sensing

Corresponding author:
Giacomo Traversa;
Email: giacomo.traversa@isp.cnr.it

cambridge.org/aog

Cryoconite holes geomorphometry, spatial distribution and radiative impact over the Hells Gate Ice Shelf, East Antarctica

Giacomo Traversa[1], Riccardo Scipinotti[2], Samuele Pierattini[3], Gianluca Bianchi Fasani[4] and Biagio Di Mauro[1]

[1]Institute of Polar Sciences, National Research Council of Italy, 20126 Milan, Italy; [2]Technical Antarctic Unit, National Agency for New Technologies, Energy and Sustainable Economic Development, 40129 Bologna, Italy; [3]Computer Systems and ICT Development, National Agency for New Technologies, Energy and Sustainable Economic Development, 50019 Sesto Fiorentino, Italy and [4]Technical Antarctic Unit, National Agency for New Technologies, Energy and Sustainable Economic Development, 00123 Rome, Italy

Abstract

Cryoconite holes are structures characteristic of the glacierised ablation areas, formed from dark sediment deposition which melt the glacier ice leading to their cylindrical structure formation. The present study focuses on an unstudied blue ice area of East Antarctica over the Hells Gate Ice Shelf in Northern Victoria Land. Taking advantage of neural network methodology applied on drone acquisitions, an automatic detection of cryoconite holes was carried out (88% of accuracy), mapping ∼3500 m^2 (0.4% fractional cover) of cryoconite holes over an area of 900 000 m^2. The surveyed area showed heterogeneity in cryoconite hole distribution, with some regions showing an area fraction of holes (regions exhibiting frozen ponds and ice bands) as high as 8%. Thanks to this detection, the spatially integrated radiative forcing of cryoconite holes over blue ice surface was estimated to be almost 1 Wm^{-2}. This estimation was based on the measured albedo difference between the two surfaces, which averages 0.31. However, the radiative forcing is strongly increased if calculated at a single cryoconite hole scale, showing an average of ∼200 Wm^{-2}. In conclusion, the present research represents a first attempt of analysing cryoconite holes as factors impacting the blue ice in Northern Victoria Land, deepening our understanding of their glaciological role at the margins of the East Antarctic Ice Sheet.

1. Introduction

A cryoconite hole (CH) is a cylindrical structure forming on the ablation areas of polar and mountain glaciers (Nordenskiöld, 1883; Cook and others, 2016; Rozwalak and others, 2022). CHs are generated by the differential ablation induced by the presence of dark sediment (i.e. cryoconite) constituted by organic and inorganic material (Takeuchi and others, 2001; Di Mauro and others, 2017). The albedo reduction induced by cryoconite sediment has the ability to melt the underlying glacier ice and to create these cylindrical structures (Hodson and others, 2005; Onuma and others, 2023). CHs are known as a biodiversity hotspot in glacial environments (Anesio and others, 2017), and they have been studied because of their ability to concentrate atmospheric pollutants (Clason and others, 2023).

On the East Antarctic Ice Sheet (EAIS), CHs have been detected over blue ice areas of glaciers and ice shelves (Brandt and others, 2009; Sinisalo and Moore, 2010; Hodson and others, 2013). These blue ice areas constitute one type of ablation areas of EAIS, presenting a negative surface mass balance (Bintanja, 1999). They cover ∼1% of the Antarctic continent (Bintanja, 1999; Winther and others, 2001; Traversa and others, 2021) and are mainly located in proximity of the coast or mountainous zones, in sloping areas (Winther and others, 2001). Their formation is linked to the effect of wind which removes and/or sublimate snow, firn and ice from the surface. Furthermore, additional loss of blue ice mass is owed to its lower albedo (0.50–0.70; Bintanja and van den Broeke, 1995; Bintanja, 1999; Reijmer and others, 2001) in respect to the surrounding snow (∼0.80; Grenfell and others, 1994; Traversa and others, 2019), increasing the available energy for sublimation and melting. Over blue ice, in Antarctica, CHs preferentially form in slight hollows where sediments and debris settle, increasing the melting rate of ice, e.g. on supraglacial ponds and surface ice bands. These bands are due to changes in ice flow caused by ice-sheet elevation changes, which leads to the incorporation of surficial material, e.g. cryoconite (Podgorny and Grenfell, 1996; Sinisalo and Moore, 2010).

CH presence over blue ice areas has been also often linked to the formation of relevant near-surface hydrologic systems (MacDonell and Fitzsimons, 2008). CH hydrology experiences cycles of temporary storage and release with consequences over glacier runoff and formation of supraglacial streams (Fountain and others, 2004; Banerjee and others, 2023). In the Arctic (Svalbard and Canadian Arctic Archipelagos), CH hydrology was also observed to be linked to weathering crust formation (Müller and Keeler, 1969), since decrease in CH water levels was attributed to cumulative increases in near-surface ice porosity, facilitated by an increasing radiative impact on the surface (Cook and others, 2016).

https://doi.org/10.1017/aog.2024.20 Published online by Cambridge University Press

In previous studies, the decrease in surface albedo and increase in absorbed solar radiation induced by CHs on glacier ice has been investigated through field observations of spectral reflectance (Takeuchi, 2002). Measurements of cryoconite optical properties have been conducted in Svalbard (Takeuchi, 2002), Himalaya (Takeuchi, 2002), Tibetan Plateau (Li and others, 2019), European Alps (Naegeli and others, 2015; Di Mauro and others, 2017; Dal Farra and others, 2018) and Greenland Ice Sheet (Tedesco and others, 2013). However, not only for radiative impact but also in a wider sense, CHs over the Antarctic ice shelves are understudied. In fact, most of the past papers were limited to McMurdo Dry Valleys Glaciers (Christner and others, 2003; Fountain and others, 2004, 2008; Porazinska and others, 2004; Bagshaw and others, 2013; Telling and others, 2014; Webster-Brown and others, 2015; MacDonell and others, 2016), with a few geographical exceptions in Dronning Maud Land, Princess Elizabeth Land, Mac. Robertson Land and certain Antarctic Islands (Brandt and others, 2009; Sinisalo and Moore, 2010; Cameron and others, 2012; Hodson and others, 2013; Obbels and others, 2016; Zdanowski and others, 2017; Samui and others, 2018; Lutz and others, 2019; Weisleitner and others, 2019, 2020). In these studies, the areas characterised for CHs include mountain glaciers (e.g. Dry Valleys) and blue ice areas (e.g. Dronning Maud Land), and only once an ice shelf, i.e. the Amery Ice Shelf blue-ice area (Mac. Robertson Land; Samui and others, 2018). In areas such as Northern Victoria Land, CHs have never been documented, despite relevant ice shelves are present (e.g. Nansen Ice Shelf, Hells Gate Ice Shelf). Accordingly, Northern Victoria Land is only the second case of CHs surveyed over blue ice areas of ice shelves after Amery Ice Shelf, making this area the most similar by a glaciological point of view. Note that the analyses over CHs of Amery Ice Shelf were limited to chemical characterisation.

The objectives of the present research are threefold: (i) to map the presence of CHs on the Hells Gate Ice Shelf (with an approach using neural network-based detection, validated against separate findings from geographic object-based image analysis); (ii) to determine the geomorphometric features of CHs and (iii) to estimate the radiative impact of CHs on blue ice of the ice shelf.

2. Materials and methods

2.1. Study area and Uncrewed Aerial Vehicle (UAV) acquisition

In the present study, we focused on the Hells Gate Ice Shelf (HGIS, Fig. 1) in the Terra Nova Bay area, located ~20 km away from the Italian Mario Zucchelli Station (MZS; 74° 41′41″S; 164°06′48″E). HGIS spans the region flanked by Vegetation Islands, Inexpressible Island (notable as the site of the snow cave from Scott's 1910–1913 expedition) and the Northern Foothills and it is known for presenting marine-ice wedges at the surface (due to ablation induced by katabatic winds, Frezzotti, 1997; Tison and others, 1998) and two alignments of ice-cored dirt cones in the western part (Salvatore and

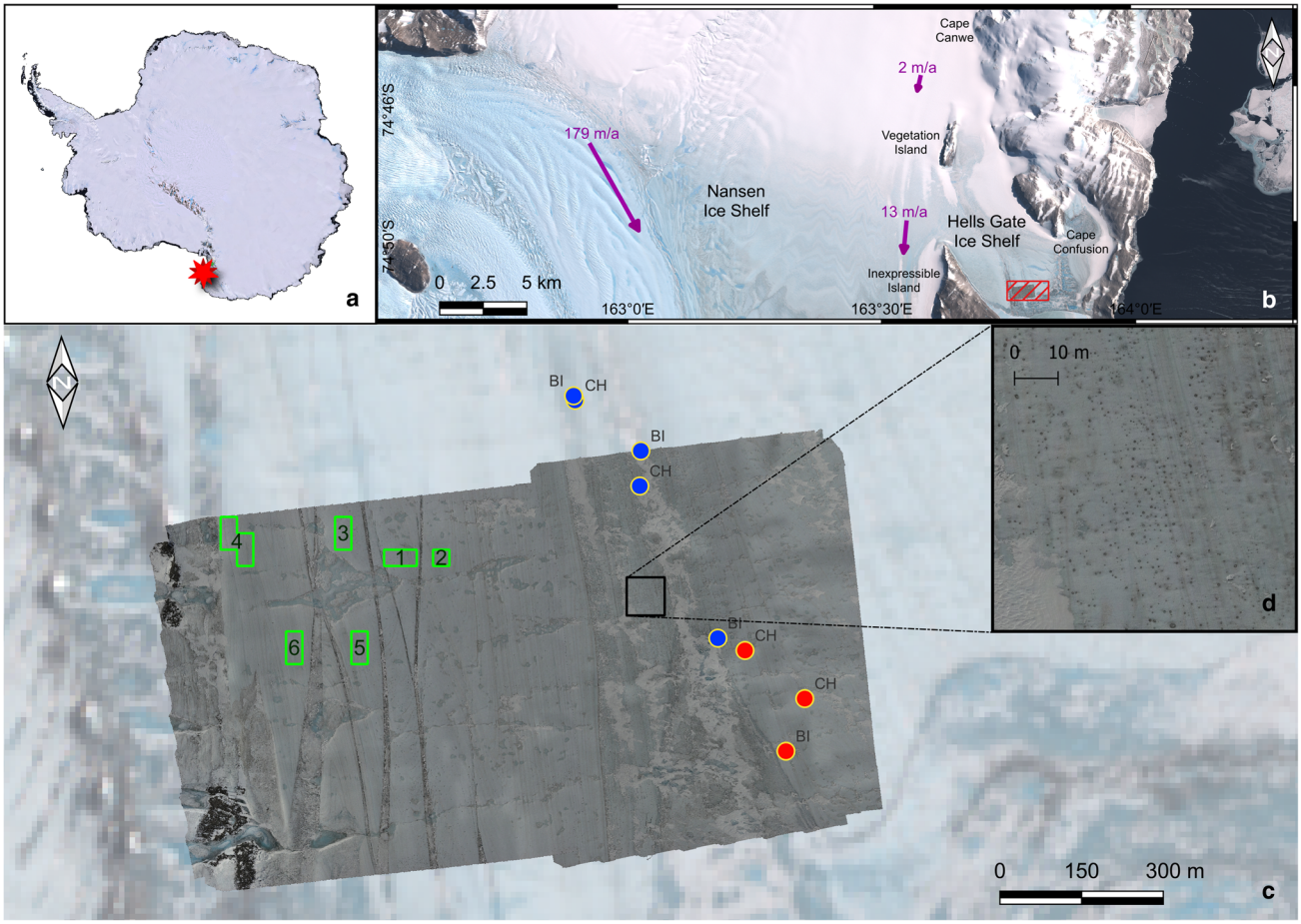

Figure 1. (a) Overview of Antarctic continent where red star shows the Hells Gate Ice Shelf location (Landsat Image Mosaic of Antarctica – LIMA in the background, Bindschadler and others, 2008). (b) Sentinel-2 true-colour image acquired on 18 November 2022 over the area of Hells Gate Ice Shelf and surrounding areas, where ice flow velocities from MEaSUREs (Making Earth System Data Records for Use in Research Environments; Rignot and others, 2017) are shown as purple arrows. (c) UAV orthophotos (red box in b) where the six areas of interest are shown in green boxes and the field spectral measurements are represented as dots in red (acquired on 13 December 2022) and blue (acquired on 30 November 2022). Measurements were taken over blue-ice (BI) and cryoconite-hole (CH) surfaces. (d) A zoom-in on the orthophoto, showing cryoconite holes.

https://doi.org/10.1017/aog.2024.20 Published online by Cambridge University Press

others, 1997) (Fig. 1). HGIS unfolds from north to south, stretching ~16.6 km in length and reaching a maximum width of 9.8 km at the latitude of Cape Confusion. The ice shelf encompasses an estimated area of ~70 km^2, albeit with some uncertainty surrounding its precise boundaries. This uncertainty arises due to the presence of snowfields and minor local glaciers along the ice shelf's periphery, particularly at its juncture with the Northern Foothills. Additionally, the western edge of HGIS meets the Nansen Ice Shelf, a connection marked at both ends of Vegetation Island extending northward to Cape Canwe and southward to Inexpressible Island (Baroni, 1988).

The aerial acquisitions were performed on 13–14 December 2022 by using the DJI M300 RTK Uncrewed Aerial Vehicle (UAV) with the mounted payload Zenmuse P1, a flexible full-frame photogrammetry camera equipped with a 35 mm lens. Only one previous study took advantage of UAVs for mapping CHs (Hodson and others, 2007). In our study, the UAV has been chosen for its enhanced flight performance due to its refined airframe and propulsion system design which gives a more efficient and stable flight, even in harsh conditions, such as in Antarctica. The missions lasted up to 37 min at a maximum speed of 23 m s^{-1} (44.7 kts) with 12 m s^{-1} (23.3 kts) of wind resistance. The camera features a 45MP sensor with a 4.4 µm pixel size and can shoot a low-noise, high sensitivity photo every 0.7 s during the flight using a TimeSync 2.0 which aligns the camera, flight controller, RTK module and gimbal at the microsecond level.

The UAV mission was planned to acquire photos of two areas of ~600 × 600 m with an estimated ground resolution of 1.51 cm px^{-1} and an overlap of the images of 80 and 70%, respectively, front and side direction. Taking into account those requirements, the flight altitude (above ice surface level) was set at 120 m and the velocity at 7 m s^{-1} yielding a flight time of ~26 min, enough to ensure a safe return of the UAV.

In a High-Performance Computing (HPC) cluster composed by four computational nodes installed at MZS, a photogrammetry software (Agisoft Metashape) was used to elaborate the photos and to obtain the orthophoto of the areas that were used for the further analysis. The first area of 600 × 594 m was acquired with 580 photos and the obtained orthophoto was 44 944 × 53 936 px with a resolution of 1.47 cm pix^{-1}. The second area of 606 × 606 m was acquired with 656 photos and the obtained orthophoto was 53 726 × 50 202 px with a resolution of 1.47 cm px^{-1}. The obtained resolution is considered high enough to identify CHs.

2.2. Cryoconite hole mapping via Neural Network (NN)

The CH mapping was performed by a two-stage Python algorithm. The first stage consisted of object detection via Neural Network (NN). Among the several models of NN capable of performing object detection (Srivastava and others, 2021; Diwan and others, 2023), we used YOLOv8 (You Only Look Once) by Ultralytics. YOLO is a cutting-edge, state-of-the-art model embedded in a platform that allows the user to do a full range of artificial intelligence tasks, including detection, segmentation, pose estimation, tracking and classification (Jiang and others, 2022; Terven and Cordova-Esparza, 2023). The software is an Open-Source-Initiative-approved open-source released under AGPL-3.0 License. In particular, in order to detect small CHs (threshold was set to $\geqslant$0.002 m^2, i.e. about three times the spatial resolution of the orthophoto) on large images such as the orthophotos obtained with the flights (~600 × 600 m), we used the SAHI (Slicing Aided Hyper Inference) library, that is a lightweight vision library for large-scale object detection, to perform inference over smaller slices of the original image and then to merge the sliced predictions (Akyon and others, 2021, 2022). In order to speed up the analysis, the YOLO environment has been deployed in the ENEA Cluster for HPC, CRESCO (Computational RESearch Centre on COmplex Systems). The NN was trained with 178 images of single CHs selected from five subsets of the orthophoto obtained with the aerial photogrammetry and the resulting model was used to detect the CHs in the whole orthophoto.

The second stage of the Python algorithm was the extraction of the best elliptical fit that approximates the shape of each detected CH by using the open-source Computer Vision library OpenCV (Bradski, 2000). The implemented procedure has four steps: (1) automatic histogram equalisation to reduce the differences of contrast between the images, (2) threshold to monochrome image needed for the elliptical fit, (3) erode filter with 3 × 3 kernel and single iteration to eliminate the single pixel artefacts which can reduce the performance of the fitting, (4) elliptical best fit with extraction of the dimensions of the two diameters and the rotation angle between the horizontal axis and the minor ellipse diameter. After delineating the mapped features in this way, we filtered the results to retain CHs over blue ice surfaces and excluded features over marine ice, snow and non-icy surfaces were removed.

Additionally, different geomorphometric parameters of CHs were calculated from this dataset, i.e. area, perimeter, roundness (defined as $4\pi \times \text{area/perimeter}^2$ and having then a value which varies between 0 and 1, where roundness of 1 corresponds to a perfect circle, while a completely ideal flat CH has a roundness of 0) and diameter/axis (depending on the roundness, if CH general shape could be approximated as a circle or not), where especially the first parameter was fundamental for the spatially integrated radiative forcing estimation.

2.3. Cryoconite hole mapping via Geographic Object-Based Image Analysis (GEOBIA)

To generate validation dataset for the NN methodology, we also detected CHs over the study area by processing the UAV orthomosaic using the Orfeo ToolBox with the Geographic Object-Based Image Analysis (GEOBIA) approach, i.e. segmenting remote-sensing imagery into image objects and evaluating their features through spatial, spectral and temporal scales (Hay and Castilla, 2008).

Initially, the orthophotos were segmented (*meanshift* algorithm), i.e. grouping neighbouring pixels together which share similar colour and have certain shape characteristics. After the segmentation, zonal statistics (mean and std dev.) were applied on the obtained shapefiles on the three RGB bands of the orthomosaics. A proxy dataset of 100 points (randomly chosen) was created. Based on the surface type (CH, blue ice, marine ice and snow) of the corresponding pixels of the image, the points have been accordingly classified (visual identification) in different classes. Then, also on this dataset the zonal statistics were calculated based on the RGB. After this step, a classifier was trained based on the labelled geometries and then the calculated model was applied in order to classify the segmented features. In conclusion, those features classified as non-CH were removed. The dataset created using the GEOBIA method needed to be visually cleaned and adjusted. Six areas of interest (AOI, 1800 m^2 on average each; Fig. 1) were identified across the orthomosaic which presented a different distribution of CHs. Focusing only on these areas, artefacts were removed and CHs adjusted, e.g. by merging those features which turned out to be cut even if they referred to a unique CH. This dataset was used to validate the corresponding CH dataset obtained by NN, evaluating its accuracy (defined as the percentage of CH features detected by NN over

https://doi.org/10.1017/aog.2024.20 Published online by Cambridge University Press

the corresponding dataset mapped via GEOBIA method) and eventual average over-/under-estimation both in terms of number of identified features and mapped area.

2.4. Field spectroscopy data and radiative forcing estimation

Reflectance measurements were acquired using a portable spectrometer covering the 400–865 nm wavelength interval (namely RoX, JB Hyperspectral Devices, Düsseldorf, Germany). The instrument is equipped with a cosine collector for measuring the hemispheric incident radiation. The reflected radiation by the surface is instead collected with a bare fibre featuring a field of view equal to 25°. The spectrometer features a full width at half maximum of 1.5 nm, and a spectral sampling of 0.68 nm. In this study, spectral reflectance has been retrieved by normalising the reflected radiation with the incident radiation. A similar set up has been already tested for snow-covered areas in the Alps (Kokhanovsky and others, 2021) and for validating satellite imaging spectroscopy data (Di Mauro and others, 2023).

Field spectroscopy data have been collected both for ice-lidded cryoconite and blue ice area in order to characterise their optical properties in the visible and near infrared part of the spectrum. For each surface type, we collected three repeated measurements (Fig. 1). The reflectance data were then used to calculate the broadband albedo of blue ice and CH. This was possible by calculating the ratio between outcoming and incoming spectral reflectance integrated in VIS-NIR wavelengths (400–865 nm).

The estimated broadband albedo was then averaged for the two classes (i.e. ice-lidded cryoconite and blue ice area) in order to obtain the average and std dev. values. In order to estimate the radiative impact of CHs on blue ice areas, we calculated the radiative forcing. The radiative forcing is defined as the enhanced absorption of solar irradiance due to surface darkening, in Wm^{-2} (Skiles and others, 2018), where surface darkening is here induced by CH presence on blue ice. For this analysis, we made use of field spectroscopy data and in particular of the albedo calculated for the two kinds of surfaces and calculated radiative forcing by multiplying albedo by the incident global radiation (as suggested in Ganey and others, 2017 for snow algae), simulated via the solar insolation calculator at *PV Lighthouse* website (using the coordinates and time on 13 December 2022 of field measurements, with default atmospheric inputs and automatically calculated solar elevations; https://www.pvlighthouse.com.au, visited on 13 March 2024). With this approach we estimated the radiative forcing at different day times, both local (i.e. a single CH scale, induced by its presence on the blue ice) and spatially integrated (i.e. surveyed area scale, based on CH distribution in respect to this area extent). This latest estimation was possible by exploiting the result of the CHs mapping from UAV over the HGIS study area.

3. Results and discussion

The section is divided into two subsections. The first subsection (section 3.1) summarises the geomorphometry and distribution of CHs over the surveyed area, as well as the validation of NN mapping with the GEOBIA approach. Based on the results of CH extent and fractional cover therein, the second subsection (section 3.2) focuses on the spectral characterisation of CHs and their radiative forcing.

3.1. Validation of NN mapping and distribution and geomorphometry of cryoconite holes

Across the six AOI described in section 2.3, the GEOBIA method identified a total of 475 CHs (~46 m^2) (Fig. 2) with a roundness of ~0.92 ± 0.09, therefore similar to perfect circles.

These CHs feature areas (diameters) ranging between 0.002 m^2 (0.057 m diameter) and 1.860 m^2 (1.555 m), with an average of 0.096 ± 0.162 m^2.

Also, the distribution significantly varies among the AOI, from a minimum of one CH every 100 m^2 (0.05% area of AOI) to 12 CHs per 100 m^2 (~1% area of AOI). In general, over all the

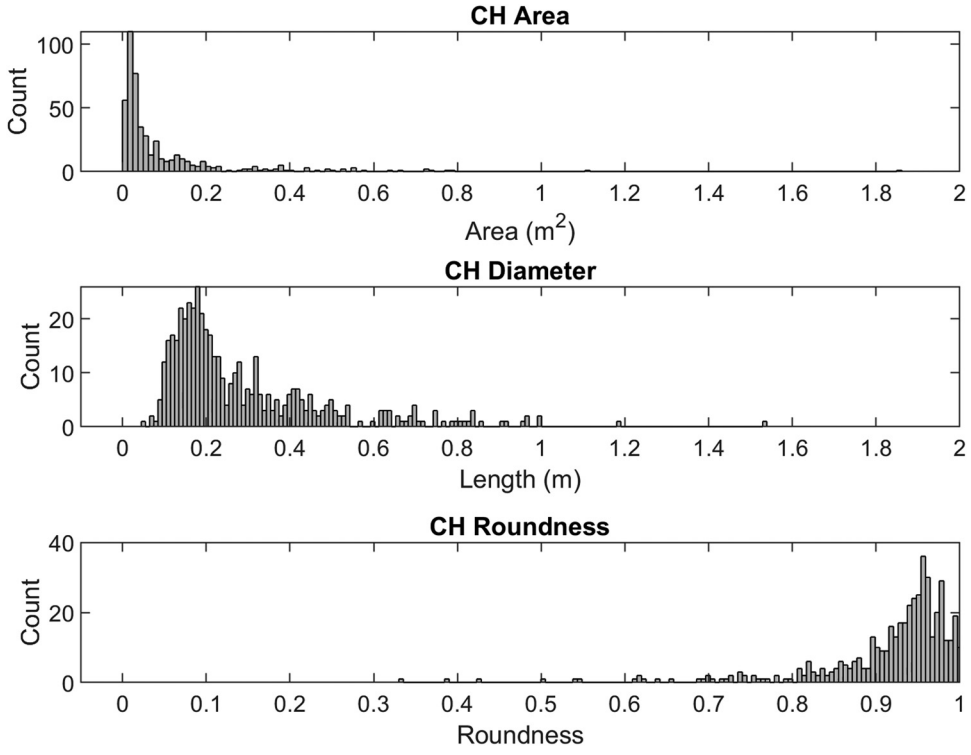

Figure 2. Histograms of area, diameter and roundness of cryoconite holes mapped through GEOBIA method over the six areas of interest of Hells Gate Ice Shelf.

https://doi.org/10.1017/aog.2024.20 Published online by Cambridge University Press

Table 1. Cryoconite holes (CHs) distribution parameters obtained using the Geographic Object-Based Image Analysis (GEOBIA) and Neural Network (NN) approaches over the six areas of interest (AOI)

AOI ID	AOI area (m^2)	No of CHs GEOBIA	No of CHs NN	CH area (m^2) GEOBIA	CH area (m^2) NN	No of CHs every 100 m^2 GEOBIA	No of CHs every 100 m^2 NN	Percentage of CH area on AOI (%) GEOBIA	Percentage of CH area on AOI (%) NN
1	1800	65	64	15.2	13.6	4	4	0.8	0.8
2	900	6	6	0.4	0.5	1	1	0.1	0.1
3	1800	73	68	7.7	5.6	4	4	0.4	0.3
4	3600	93	97	4.2	5.0	3	3	0.1	0.1
5	1800	217	199	17.2	17.3	12	11	1.0	1.0
6	1800	21	18	1.1	1.2	1	1	0.1	0.1

AOI, we found an average of four CHs per 100 m^2 with a CH area covering 0.4% of AOI.

On the other hand, similar results were obtained applying the NN approach. In fact, out of the 475 CHs detected with GEOBIA, 419 were also identified using NN (88% of accuracy), with other 33 non-CH features mapped (7% of the total features detected with NN). For the 419 CHs detected, a CH area of 43 m^2 was estimated against an area of 41 m^2 from GEOBIA (6% of area overestimation). The other parameters slightly differ from the ones obtained by the GEOBIA approach. Dimensionally, the CHs by NN detected show an area ranging between 0.003 m^2 (0.070 m diameter) and 2.340 m^2 (1.695 m diameter), with an average again of 0.096 ± 0.129 m^2 (diameter of 0.350 ± 0.405 m). All the other parameters are included in Table 1.

In general, the areas and diameters here calculated are in line with the results obtained in the McMurdo Dry Valleys (distant about 300 km north of HGIS), where diameters of 0.050–0.1450 m were found (Fountain and others, 2004). Therefore, our results from HGIS supports previous studies, which found Antarctic CHs (decimetre scale) to be larger than CHs from the Arctic and the Third Pole (centimetre scale; Takeuchi and others, 2001, 2018; Tedesco and others, 2013; Onuma and others, 2023). The final results obtained by NN approach across the entire study area, which covers ~900 000 m^2, identified almost 33 000 CHs, whose areas total ~3500 m^2. Therefore, out of the entire analysed area, an average of four CHs every 100 m^2 and a CH percent cover of 0.4% were calculated, in accordance to the average statistics obtained for the six AOI with GEOBIA. Nevertheless, the maximum and minimum (number and percent cover of CH) for this dataset varied from the GEOBIA dataset. In fact, the maximum CHs encountered every 100 m^2 is 84 and the percent cover of CH reaches a minimum of 0.002% (single small CH) and a maximum of 8.1% (Fig. 3).

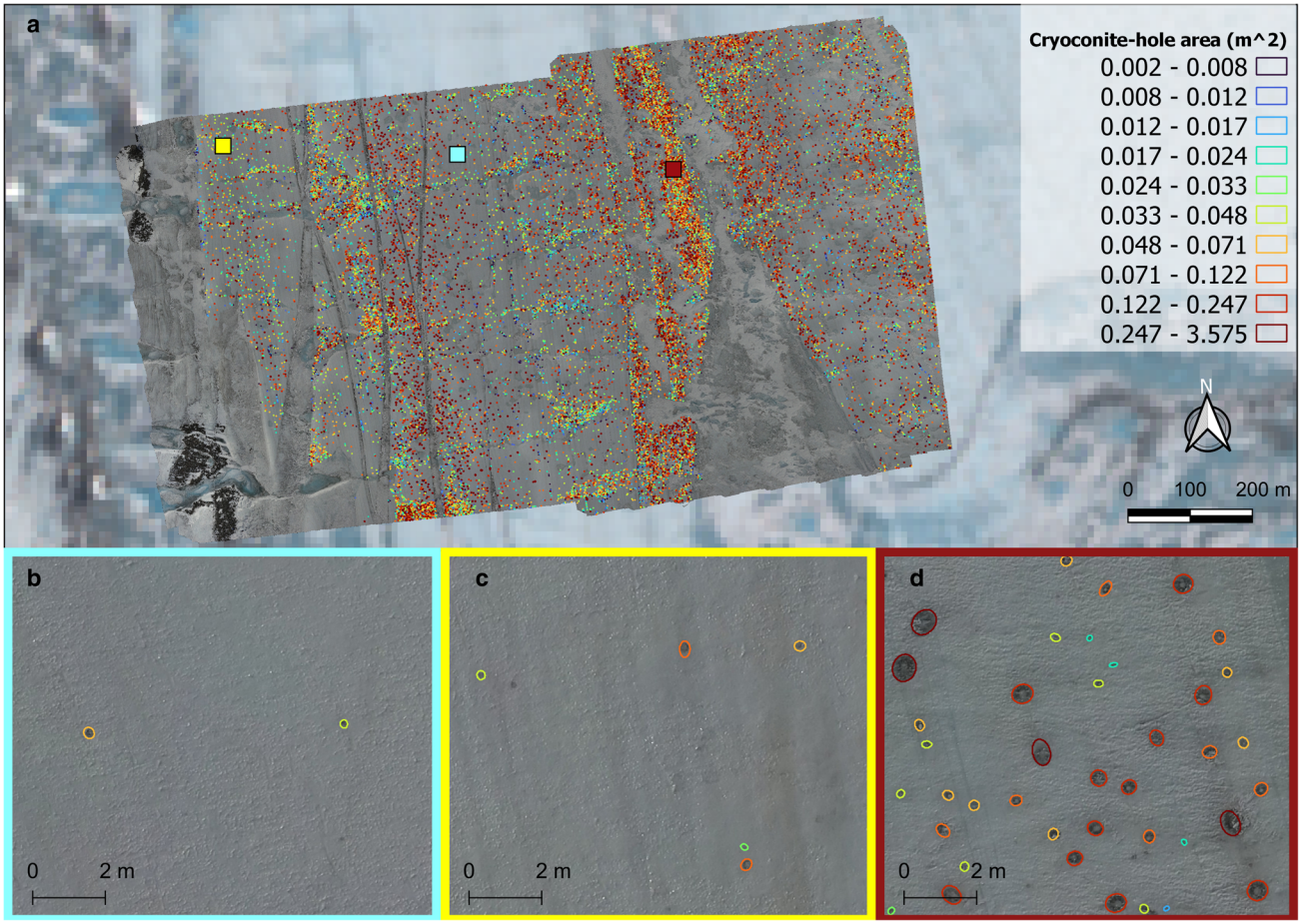

Figure 3. (a) Distribution of cryoconite holes (CHs) across the surveyed area over Hells Gate Ice Shelf (HGIS) with colour scale based on CH size. Sentinel-2 true-colour image (18 November 2022) in the background. Below, three zoom in of three sub-areas (coloured squares in a) presenting different CH distribution in respect to the surrounding blue ice: (b) low frequency (~0.1%, blue box), (c) average frequency (~0.4%, yellow box) and (d) high frequency (~6.0%, red box).

https://doi.org/10.1017/aog.2024.20 Published online by Cambridge University Press

These findings show slightly lower fractional cover of CH over glacier ice compared to the few other studies in Antarctica, both in the McMurdo Dry Valleys, which showed percent average values between 3.4 and 6.4%, respectively over Taylor and Howard Glaciers (Fountain and others, 2004), and over another blue ice area investigated of the Amery Ice Shelf near the Vestfold Hills (EAIS). In fact, this latest area shows percent covers up to 16% (Hodson and others, 2013). Nevertheless, similar values (0.4% on average over the entire area, Fig. 4) were found over the Longyearbreen in Svalbard Archipelago, surveyed via UAVs, showing 0.4% of CH cover, even if there each feature shows diameter of an order of magnitude lower in respect to HGIS (Hodson and others, 2007). However, the 0.4% average cover here derives from a strongly heterogeneous spatial distribution, with most of the surveyed area presenting few CHs every 100 m^2 (<10 CHs or <2% of fractional cover; blueish areas in Fig. 4).

Only a few spots, mostly located in proximity of supraglacial frozen ponds or inside of them (yellow/red areas in the middle-western portion of the area, Fig. 4), present CH cover significantly higher, especially in terms of number of CHs, with more than 20 CHs every 100 m^2 (>3% fractional cover, yellowish pixels in Fig. 4) up to about 50 CHs (5% fractional cover, red pixels in Fig. 4a). Additionally, high abundance was found in the zones slightly to the east and to the north of the marine-ice wedge (20–30 CHs every 100 m^2, 2–4% fractional cover) and along ice bands. All these areas, i.e. supraglacial ponds, marine-ice wedges and ice bands share the same topographic characteristics, i.e. being slight hollows. In fact, as demonstrated in previous studies over blue and sea ice (Podgorny and Grenfell, 1996; Sinisalo and Moore, 2010), the lower surface of these landforms facilitates windblown rock particles to settle on the ice surface, leading to CH formation and thus affecting also the CH distribution. This hypothesis corroborates a major role of the topography rather than wind direction and intensity or sediment sources, especially over HGIS where wind direction is very constant (westing for about 80% of time in summer 2022–2023; source: Manuela Automatic Weather Station over Inexpressible Island; AMRC, SSEC, UW-Madison) and sediment sources are mainly granitoids from Inexpressible Island, Vegetation Island and the surrounding Transantarctic Mountains (Tingey, 1991).

3.2. Radiative forcing induced by cryoconite holes

The reflectance measurements acquired over the study area of HGIS provided strongly different results for blue ice and CH surfaces (Fig. 5).

In fact, broadband albedo of blue ice estimated out of the three measurements provided a value of 0.60 ± 0.08, in accordance with previous results (Bintanja and van den Broeke, 1995; Bintanja, 1999; Reijmer and others, 2001; Traversa and others, 2021) and CH albedo turned out to be almost halved in respect to blue ice, equal to 0.29 ± 0.07. This result is higher than previous measurements made in other regions for CHs showing albedo <0.20 (Takeuchi and others, 2001; Takeuchi, 2002; Rossini and others, 2023). The reason behind is the presence of the ice of the refrozen lid (with an average thickness calculated over the CHs sampled over HGIS of 8 ± 2 cm) which covers almost the entirety of the present CHs (Fig. 5b). This lid is affected by the influence of the sediment (~30 cm deep under a layer of air and water, Fig. 5a), making it darker in respect to the blue ice (and more similar to e.g. dirty glacier ice; Fugazza and others, 2016; Di

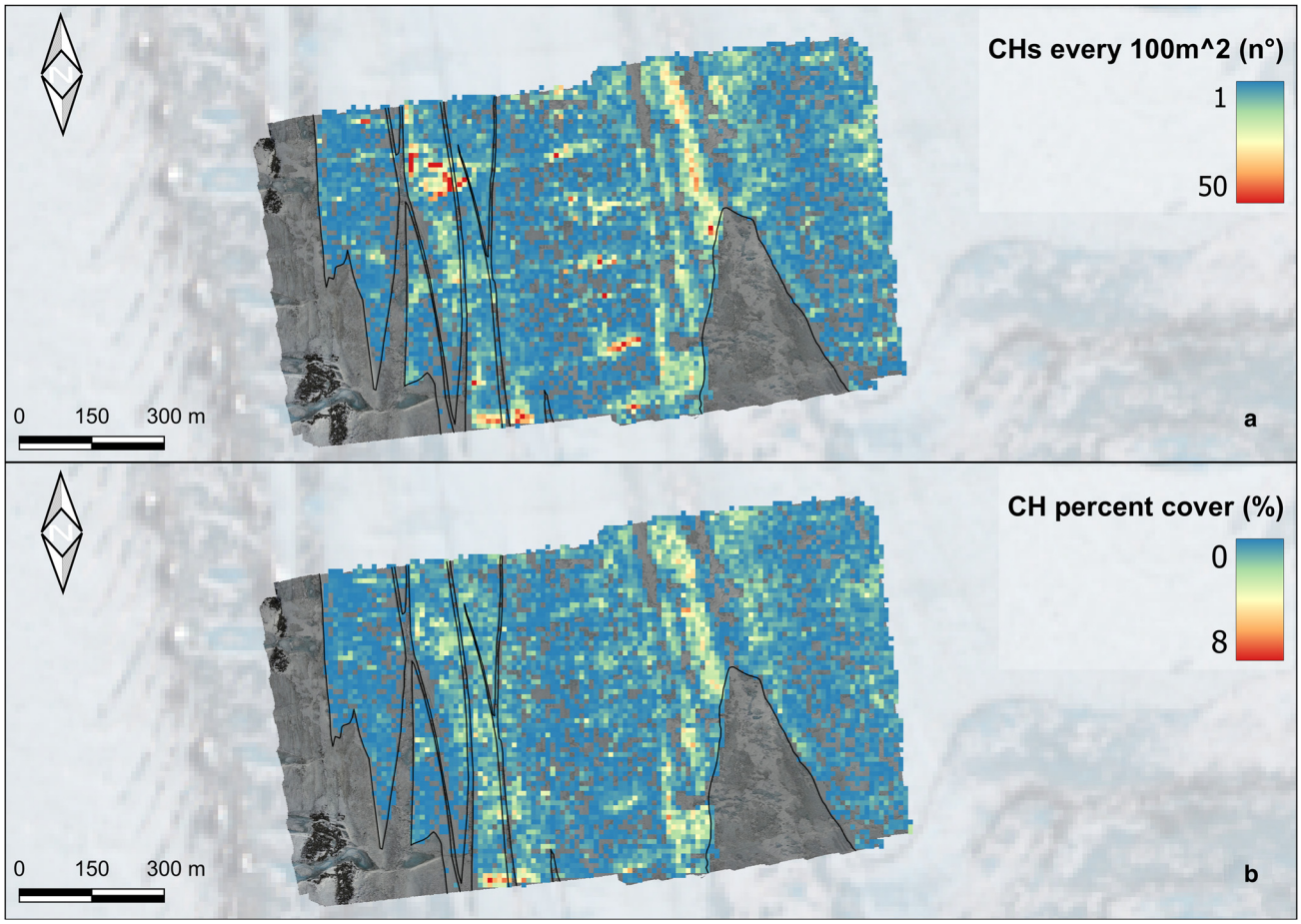

Figure 4. Heat maps of the surveyed area over Hells Gate Ice Shelf based on the number of cryoconite holes (CHs, a) and area covered by CH (b). Both the heat maps have a spatial resolution of 10 m. The black lines outline the marine ice wedges.

https://doi.org/10.1017/aog.2024.20 Published online by Cambridge University Press

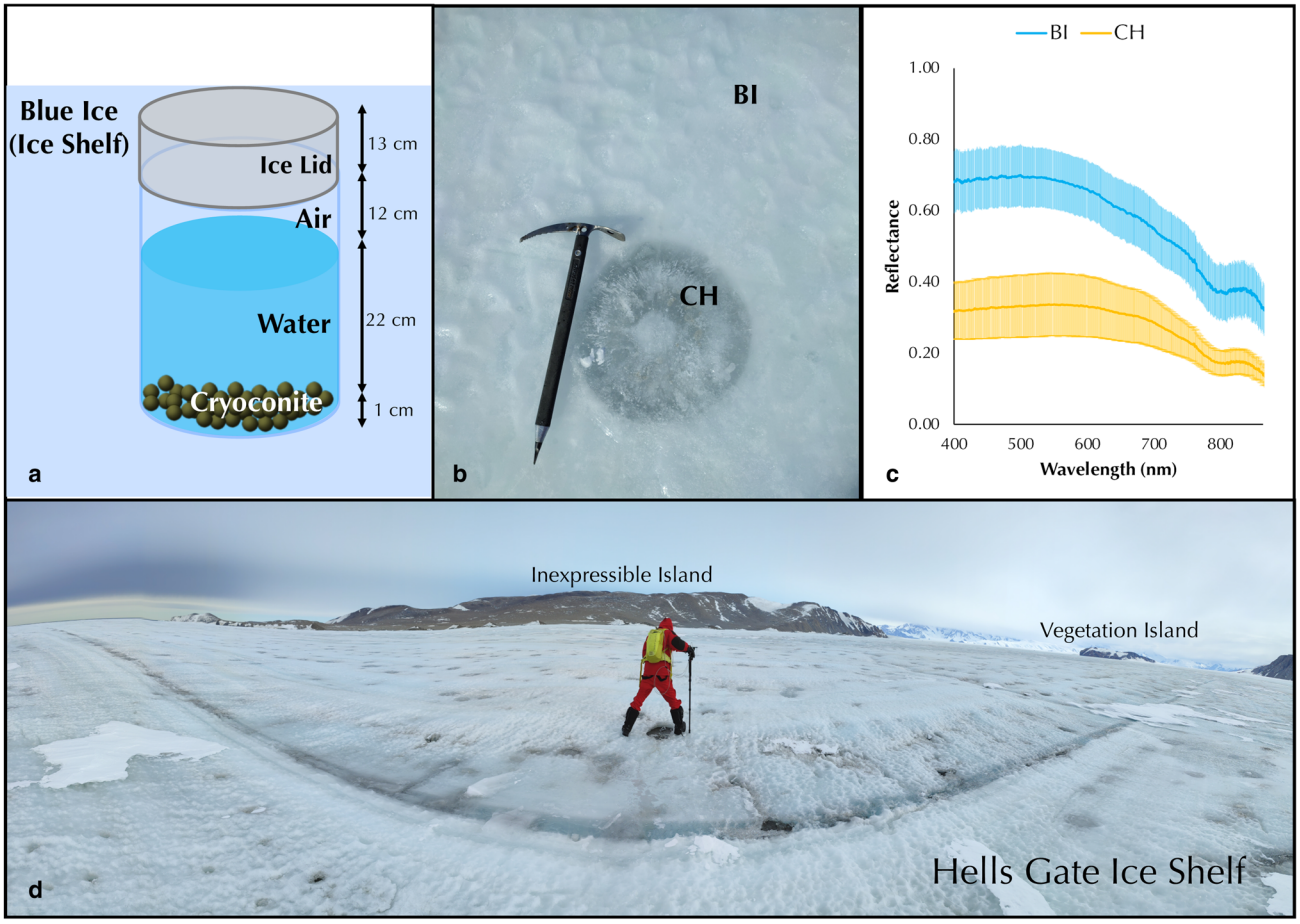

Figure 5. (a) Cryoconite-hole (CH) idealised model showing the different measured thicknesses of each CH component (averages calculated from 25 CHs sampled during the campaign over Hells Gate Ice Shelf – HGIS, Nansen Ice Shelf and Priestley Glacier); (b) upper view of a CH (photo taken on 13 December 2022 over HGIS) and the surrounding blue ice (BI); (c) different spectra (averages calculated from six measurements, see Fig. 1) of BI and CH between 400 and 865 nm acquired using the RoX spectrometer and (d) field wide-angle view of a portion of HGIS blue ice area where several CHs are present (photo taken on 13 December 2022).

Mauro and Fugazza, 2022), especially affecting its reflectance in the visible wavelengths (Fig. 5c), but providing higher albedo in respect to bare cryoconite. Here, the CH spectrum shows a similar trend to the blue ice one, even if the visible reflectance tends to be lower by about 0.4. This difference becomes almost halved at higher wavelengths (near-infrared, >800 nm). These observed

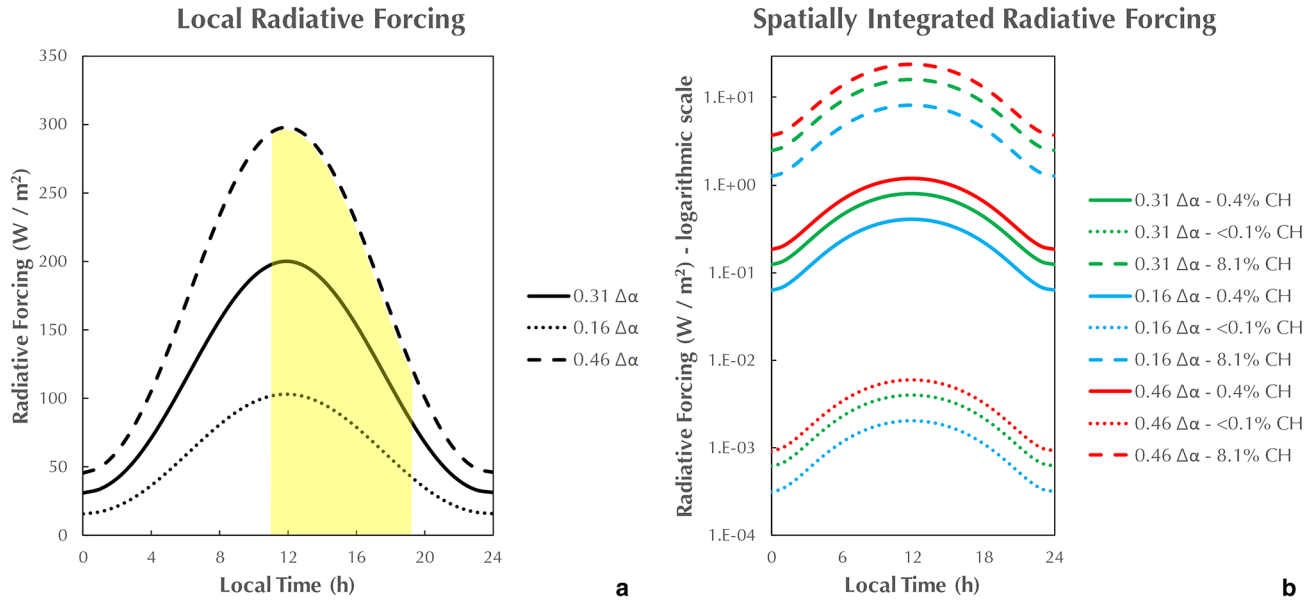

Figure 6. Daily variation of local (a) and spatially integrated (b) radiative forcing induced by cryoconite hole (CH) presence. Different albedo differences (Δα) refer to the maximum (0.46) and the minimum difference (0.16) of albedo between blue ice and CH, as well as between their average values (0.31). In (b) are also shown the variation of radiative forcing as a function of increasing cover of CH surface over blue ice areas, here calculated from a minimum <0.1% to a maximum of 8.1%, with an average of 0.4%. The yellow area refers to the corresponding span of time during which field spectral measurements were acquired.

https://doi.org/10.1017/aog.2024.20 Published online by Cambridge University Press

differences between blue ice and CHs correspond to an average broadband albedo difference of 0.31 (with a maximum and minimum albedo differences respectively of 0.46 and 0.16), from which we could estimate the local and spatially integrated radiative forcing due to CHs over ice-shelf surface (on the base of minimum, average and maximum CH percent cover over the entire study area, respectively: 0.002, 0.4 and 8.1% (Fig. 6).

Locally, the radiative forcing induced by the presence of a CH over blue ice surface (single CH scale) at the maximum incident global radiation (at 12.00 hours local time) was estimated to be equal to 200.2 Wm^{-2}, considering average albedo difference between blue ice and CH of 0.31. The local radiative forcing when considering the minimum and maximum albedo differences was instead 103.0 and 297.5 Wm^{-2} respectively (Fig. 6a). However, considering the spatially integrated radiative forcing, which depends on the percent cover of CH surface in a given area (calculated minimum of 0.002%, maximum of 8.1% and average 0.4%; section 3.1), the situation significantly changes (Fig. 6b). With an albedo difference of 0.31, the radiative forcing ranges between 0–16 Wm^{-2} (minimum–maximum), and 0.8 Wm^{-2} for an average CH cover. However, in the case of maximum albedo difference and maximum CH percent cover, the radiative forcing reaches the high value of 23.8 Wm^{-2}.

When compared to other light-absorbing-particle radiative-forcing effects on snow or ice, the results obtained here for the spatially integrated effect induced by CHs are similar to the forcing caused by algal presence over ice (dependent on the biomass), which provided an average value of 0.4 Wm^{-2} over the Greenland Ice Sheet for 10 000 cells case (Halbach and others, 2022) and of ~0.1–2.5 Wm^{-2} over North American glaciers (Engstrom and Quarmby, 2023). However, over snow in Alaska, much higher results were obtained for red-algae and dust, especially at higher abundance, leading to a spatially integrated average of 21.6 ± 5.9 Wm^{-2} (Ganey and others, 2017). The main reason for this difference could be found in the higher albedo values of snow (leading to higher albedo difference and higher radiative forcing) which is more influenced by light-absorbing-particle presence in respect to ice. Nevertheless, the ranges of radiative forcing obtained in the present analysis are in line with the results calculated in general for light-absorbing particles in other regions of the Earth (Skiles and others, 2018), even if, in this context, the situation differs from the other cases. In fact, over HGIS most of the CHs present an ice lid which mitigates the albedo reduction (albedo of 0.29 ± 0.07) caused by cryoconite debris presence. If a larger portion of CHs do not show any ice lid, the albedo difference and therefore also the radiative forcing would be higher. Additionally, the dominant surrounding surface on HGIS is blue ice (albedo of ~0.60) and not snow (~0.80), whose presence again mitigates a stronger radiative forcing than snow. Secondly, as demonstrated in the present study, the fractional cover of CHs over blue ice especially plays a key role in the radiative-forcing evaluation. In fact, if spatially integrated over the surveyed blue-ice area extent (surveyed area scale), the radiative forcing induced by CH presence is decreased by two orders of magnitude, from ~200 Wm^{-2} (local, at a single cryoconite scale, with 0.31 albedo difference) to ~1 Wm^{-2} (spatially integrated).

4. Conclusion

The present study describes for the first time cryoconite hole (CH) presence over the Hells Gate Ice Shelf. This analysis is the first observation of CHs in regions of the Northern Victoria Land (EAIS). The research utilised aerial photogrammetry and geographical-chronological corresponding spectroscopy measurements. In detail, these acquisitions allowed us to estimate the reflectance and broadband albedo of the ice lid of CHs and of the surrounding blue ice together with CH cover extent, for radiative forcing estimation.

The CH cover was estimated to be ~3500 m^2 (0.4% of the 0.9 km^2 mapped area) for about 33 000 CHs detected with 88% accuracy. However, the CH distribution across the area was found to be strongly heterogeneous, with a general cover <1%, but showing spots with concentrations up to 8%, mostly located over supraglacial frozen ponds, ice bands or in proximity of marine-ice transition. Possibly, these higher concentrations could be linked with the stronger mass loss occurring over these surfaces leading to depression areas, facilitating the settlement of sediments and debris over ice.

Together with CH cover estimation, the albedo difference between blue ice and CHs (equal to +0.31 on average) led to a spatially integrated radiative forcing caused by CH ice-lid presence up to +23.8 Wm^{-2}, with an average of 0.8 Wm^{-2}. However, the local (single CH scale) radiative forcing showed much higher impact, with instant values at the maximum incident global radiation equal to 200.2 Wm^{-2} (average albedo difference of 0.31) and 103.0 and 297.5 Wm^{-2} for minimum and maximum albedo differences between the two ice surfaces. Therefore, we demonstrated the possible impact of CH presence over the surface energy balance of the ice shelf and how the CH extent (in terms of fractional cover) plays a key role. In conclusion, in those areas where the fractional cover of CHs was supposed to be impactful, the radiative roles of CHs would be relevant and worthy of study (especially in regions where the light-absorbing particles influence is less studied, e.g. HGIS), and may have additional implications for the hydrology of glaciers and ice shelves (Fountain and others, 2004; Cook and others, 2016).

Future efforts would focus on the biological and mineralogical characterisation of the cryoconite of HGIS, as well as of other glaciers and ice shelves of the Northern Victoria Land (e.g. Nansen Ice Shelf, Priestley Glacier), with the aim of inferring the origin of this sediment and eventually its link with CH genesis.

These analyses would help in a better understanding of CH characterisation over these few studied areas and of the role of biological communities (in consideration of its abundance inside CHs) over surface mass and energy balance of ice at the margins of the EAIS.

Data. Data reported in this manuscript are available on request.

Acknowledgements. The authors are thankful to the National Antarctic Research Program of Italy (PNRA), for funding the fellowship of Dr G. Traversa, and to Professor B. Leoni (University of Milano-Bicocca) and the alpine guides and helicopter pilots of Mario Zucchelli Station (MZS) for having supported the field activities. This study was supported by the project *Bio-Geo Albedo feedback at Antarctic Ice-Sheet margins* (no. PNRA18_00222) and the PNRA. The computing resources and the related technical support used for this work have been provided by CRESCO/ENEAGRID High Performance Computing infrastructure and its staff (Iannone and others, 2019). CRESCO/ENEAGRID High Performance Computing infrastructure is funded by ENEA, the Italian National Agency for New Technologies, Energy and Sustainable Economic Development and by Italian and European research programmes, see http://www.cresco.enea.it/english for information.

Author contributions. G. T. and B. D. M. conceived the idea of this work and wrote most of the paper and collected data on reflectance measurements. G. T. performed most of the calculations. R. S. and S. P. collected data on UAV acquisitions. R. S., S. P. and G. B. F. performed photogrammetry processing and NN mapping and contributed to writing the paper.

References

Akyon FC and 5 others (2021) SAHI: a lightweight vision library for performing large scale object detection and instance segmentation. https://doi.org/10.5281/zenodo.5718950

https://doi.org/10.1017/aog.2024.20 Published online by Cambridge University Press

Akyon FC, Altinuc SO and Temizel A (2022) Slicing aided hyper inference and fine-tuning for small object detection. *2022 IEEE International Conference on Image Processing (ICIP)*. IEEE, 966–970. doi: 10.1109/ICIP46576.2022.9897990

Anesio AM, Lutz S, Chrismas NAM and Benning LG (2017) The microbiome of glaciers and ice sheets. *NPJ Biofilms and Microbiomes* **3**(1), 1–11. doi: 10.1038/s41522-017-0019-0

Bagshaw EA and 5 others (2013) Do cryoconite holes have the potential to be significant sources of C, N, and P to downstream depauperate ecosystems of Taylor Valley, Antarctica? *Arctic, Antarctic, and Alpine Research* **45**(4), 440–454. doi: 10.1657/1938-4246-45.4.440

Banerjee A and 5 others (2023) A scaling relation for cryoconite holes. *Geophysical Research Letters* **50**(22), e2023GL104942. doi: 10.1029/2023GL104942

Baroni C (1988) The Hells Gate and Backstairs Passage Ice Shelves, Victoria Land-Antarctica. *Memorie della Società Geologica Italiana* **43**, 123–144.

Bindschadler R and 8 others (2008) The Landsat image mosaic of Antarctica. *Remote Sensing of Environment* **112**(12), 4214–4226. doi: 10.1016/j.rse.2008.07.006

Bintanja R (1999) On the glaciological, meteorological, and climatological significance of Antarctic blue ice areas. *Reviews of Geophysics* **37**(3), 337–359.

Bintanja R and van den Broeke MR (1995) The surface energy balance of Antarctic snow and blue ice. *Journal of Applied Meteorology and Climatology* **34**(4), 902–926.

Bradski G (2000) The openCV library. *Dr Dobb's Journal: Software Tools for the Professional Programmer* **25**(11), 120–123.

Brandt O, Taurisano A, Giannopoulos A and Kohler J (2009) What can GPR tell us about cryoconite holes? 3D FDTD modeling, excavation and field GPR data. *Cold Regions Science and Technology* **55**(1), 111–119. doi: 10.1016/j.coldregions.2008.06.002

Cameron KA, Hodson AJ and Osborn AM (2012) Structure and diversity of bacterial, eukaryotic and archaeal communities in glacial cryoconite holes from the Arctic and the Antarctic. *FEMS Microbiology Ecology* **82**(2), 254–267.

Christner BC, Kvitko BH and Reeve JN (2003) Molecular identification of Bacteria and Eukarya inhabiting an Antarctic cryoconite hole. *Extremophiles* **7**(3), 177–183. doi: 10.1007/s00792-002-0309-0

Clason CC and 22 others (2023) Global variability and controls on the accumulation of fallout radionuclides in cryoconite. *Science of the Total Environment* **894**, 164902. doi: 10.1016/j.scitotenv.2023.164902

Cook JM, Hodson AJ and Irvine-Fynn TDL (2016) Supraglacial weathering crust dynamics inferred from cryoconite hole hydrology. *Hydrological Processes* **30**(3), 433–446. doi: 10.1002/hyp.10602

Dal Farra A and 5 others (2018) Spectral signatures of submicron scale light-absorbing impurities in snow and ice using hyperspectral microscopy. *Journal of Glaciology* **64**(245), 377–386.

Di Mauro B and Fugazza D (2022) Pan-Alpine glacier phenology reveals lowering albedo and increase in ablation season length. *Remote Sensing of Environment* **279**, 113119.

Di Mauro B and 7 others (2017) Impact of impurities and cryoconite on the optical properties of the Morteratsch Glacier (Swiss Alps). *The Cryosphere* **11**(6), 2393–2409.

Di Mauro B and 14 others (2023) Evaluation of PRISMA products over snow in the Alps and Antarctica. *ESS Open Archive*. December 27, 2023. doi: 10.22541/essoar.170365189.95440911/v1

Diwan T, Anirudh G and Tembhurne JV (2023) Object detection using YOLO: challenges, architectural successors, datasets and applications. *Multimedia Tools and Applications* **82**(6), 9243–9275. doi: 10.1007/s11042-022-13644-y

Engstrom CB and Quarmby LM (2023) Satellite mapping of red snow on North American glaciers. *Science Advances* **9**(47), eadi3268. doi: 10.1126/sciadv.adi3268

Fountain AG, Tranter M, Nylen TH, Lewis KJ and Mueller DR (2004) Evolution of cryoconite holes and their contribution to meltwater runoff from glaciers in the McMurdo Dry Valleys, Antarctica. *Journal of Glaciology* **50**(168), 35–45.

Fountain AG, Nylen TH, Tranter M and Bagshaw E (2008) Temporal variations in physical and chemical features of cryoconite holes on Canada Glacier, McMurdo Dry Valleys, Antarctica. *Journal of Geophysical Research: Biogeosciences* **113**(G1), 2007JG000430. doi: 10.1029/2007JG000430

Frezzotti M (1997) Ice front fluctuation, iceberg calving flux and mass balance of Victoria Land glaciers. *Antarctic Science* **9**(1), 61–73.

Fugazza D, Senese A, Azzoni RS, Maugeri M and Diolaiuti GA (2016) Spatial distribution of surface albedo at the Forni Glacier (Stelvio National Park, Central Italian Alps). *Cold Regions Science and Technology* **125**, 128–137. doi: 10.1016/j.coldregions.2016.02.006

Ganey GQ, Loso MG, Burgess AB and Dial RJ (2017) The role of microbes in snowmelt and radiative forcing on an Alaskan icefield. *Nature Geoscience* **10**(10), 754–759.

Grenfell TC, Warren SG and Mullen PC (1994) Reflection of solar radiation by the Antarctic snow surface at ultraviolet, visible, and near-infrared wavelengths. *Journal of Geophysical Research: Atmospheres* **99**(D9), 18669–18684.

Halbach L and 14 others (2022) Pigment signatures of algal communities and their implications for glacier surface darkening. *Scientific Reports* **12**(1), 17643. doi: 10.1038/s41598-022-22271-4

Hay GJ and Castilla G (2008) Geographic Object-Based Image Analysis (GEOBIA): a new name for a new discipline. In Blaschke T, Lang S and Hay GJ (eds), *Object-Based Image Analysis: Spatial Concepts for Knowledge-Driven Remote Sensing Applications*. Berlin, Heidelberg: Springer, pp. 75–89. doi: 10.1007/978-3-540-77058-9_4

Hodson AJ, Mumford PN, Kohler J and Wynn PM (2005) The High Arctic glacial ecosystem: new insights from nutrient budgets. *Biogeochemistry* **72**, 233–256.

Hodson A and 10 others (2007) A glacier respires: quantifying the distribution and respiration CO_2 flux of cryoconite across an entire Arctic supraglacial ecosystem. *Journal of Geophysical Research: Biogeosciences* **112**(G4), 2007JG000452. doi: 10.1029/2007JG000452

Hodson A, Paterson H, Westwood K, Cameron K and Laybourn-Parry J (2013) A blue-ice ecosystem on the margins of the East Antarctic ice sheet. *Journal of Glaciology* **59**(214), 255–268.

Iannone F and 9 others (2019) CRESCO ENEA HPC clusters: a working example of a multifabric GPFS Spectrum Scale layout. *2019 International Conference on High Performance Computing & Simulation (HPCS)*. IEEE, 1051–1052. doi: 10.1109/HPCS48598.2019.9188135

Jiang P, Ergu D, Liu F, Cai Y and Ma B (2022) A review of Yolo algorithm developments. *Procedia Computer Science* **199**, 1066–1073.

Kokhanovsky A, Di Mauro B, Garzonio R and Colombo R (2021) Retrieval of dust properties from spectral snow reflectance measurements. *Frontiers in Environmental Science* **9**, 644551. doi: 10.3389/fenvs.2021.644551

Li Y and 8 others (2019) Cryoconite on a glacier on the north-eastern Tibetan plateau: light-absorbing impurities, albedo and enhanced melting. *Journal of Glaciology* **65**(252), 633–644.

Lutz S, Ziolkowski LA and Benning LG (2019) The biodiversity and geochemistry of cryoconite holes in Queen Maud Land, East Antarctica. *Microorganisms* **7**(6), 160.

MacDonell S and Fitzsimons S (2008) The formation and hydrological significance of cryoconite holes. *Progress in Physical Geography: Earth and Environment* **32**(6), 595–610. doi: 10.1177/0309133308101382

MacDonell S, Sharp M and Fitzsimons S (2016) Cryoconite hole connectivity on the Wright Lower Glacier, McMurdo Dry Valleys, Antarctica. *Journal of Glaciology* **62**(234), 714–724.

Müller F and Keeler CM (1969) Errors in short-term ablation measurements on melting ice surfaces. *Journal of Glaciology* **8**(52), 91–105. doi: 10.3189/S0022143000020785

Naegeli K, Damm A, Huss M, Schaepman M and Hoelzle M (2015) Imaging spectroscopy to assess the composition of ice surface materials and their impact on glacier mass balance. *Remote Sensing of Environment* **168**, 388–402. doi: 10.1016/j.rse.2015.07.006

Nordenskiöld AE (1883) Nordenskiöld on the Inland Ice of Greenland. *Science* **2**(44), 732–738. doi: 10.1126/science.ns-2.44.732

Obbels D and 9 others (2016) Bacterial and eukaryotic biodiversity patterns in terrestrial and aquatic habitats in the Sør Rondane Mountains, Dronning Maud Land, East Antarctica. *FEMS Microbiology Ecology* **92**(6), fiw041.

Onuma Y, Fujita K, Takeuchi N, Niwano M and Aoki T (2023) Modelling the development and decay of cryoconite holes in northwestern Greenland. *The Cryosphere* **17**(8), 3309–3328. doi: 10.5194/tc-17-3309-2023

Podgorny IA and Grenfell TC (1996) Absorption of solar energy in a cryoconite hole. *Geophysical Research Letters* **23**(18), 2465–2468. doi: 10.1029/96GL02229

Porazinska DL and 5 others (2004) The biodiversity and biogeochemistry of cryoconite holes from McMurdo Dry Valley Glaciers, Antarctica. *Arctic, Antarctic, and Alpine Research* **36**(1), 84–91. doi: 10.1657/1523-0430(2004)036[0084:TBABOC]2.0.CO;2

https://doi.org/10.1017/aog.2024.20 Published online by Cambridge University Press

Reijmer CH, Bintanja R and Greuell W (2001) Surface albedo measurements over snow and blue ice in thematic mapper bands 2 and 4 in Dronning Maud Land, Antarctica. *Journal of Geophysical Research: Atmospheres* **106** (D9), 9661–9672.

Rignot E, Mouginot J and Scheuchl, B (2017) MEaSUREs InSARbased Antarctica ice velocity map, version 2. *Boulder CO NASA DAAC Natl. Snow Ice Data Cent. [data set]*. doi: 10.5067/D7GK8F5J8M8R

Rossini M and 8 others (2023) Mapping surface features of an Alpine glacier through multispectral and thermal drone surveys. *Remote Sensing* **15**(13), 3429. doi: 10.3390/rs15133429

Rozwalak P and 32 others (2022) Cryoconite – from minerals and organic matter to bioengineered sediments on glacier's surfaces. *Science of The Total Environment* **807**, 150874. doi: 10.1016/j.scitotenv.2021.150874

Salvatore MC, Bondesan A, Meneghel M, Baroni C and Orombelli G (1997) Geomorphological sketch map of the Evans Cove area (Victoria Land, Antarctica). *Geografia Fisica e Dinamica Quaternaria* **20**, 283–290.

Samui G, Antony R and Thamban M (2018) Chemical characteristics of hydrologically distinct cryoconite holes in coastal Antarctica. *Annals of Glaciology* **59**(77), 69–76.

Sinisalo A and Moore JC (2010) Antarctic blue ice areas – towards extracting palaeoclimate information. *Antarctic Science* **22**(2), 99–115. doi: 10.1017/S0954102009990691

Skiles SM, Flanner M, Cook JM, Dumont M and Painter TH (2018) Radiative forcing by light-absorbing particles in snow. *Nature Climate Change* **8**(11), 964–971.

Srivastava S and 5 others (2021) Comparative analysis of deep learning image detection algorithms. *Journal of Big Data* **8**(1), 66. doi: 10.1186/s40537-021-00434-w

Takeuchi N (2002) Optical characteristics of cryoconite (surface dust) on glaciers: the relationship between light absorbency and the property of organic matter contained in the cryoconite. *Annals of Glaciology* **34**, 409–414. doi: 10.3189/172756402781817743

Takeuchi N, Kohshima S and Seko K (2001) Structure, formation, and darkening process of albedo-reducing material (cryoconite) on a Himalayan Glacier: a granular algal mat growing on the Glacier. *Arctic, Antarctic, and Alpine Research* **33**(2), 115–122. doi: 10.1080/15230430.2001.12003413

Takeuchi N and 6 others (2018) Temporal variations of cryoconite holes and cryoconite coverage on the ablation ice surface of Qaanaaq Glacier in northwest Greenland. *Annals of Glaciology* **59**(77), 21–30. doi: 10.1017/aog.2018.19

Tedesco M, Foreman CM, Anton J, Steiner N and Schwartzman T (2013) Comparative analysis of morphological, mineralogical and spectral properties of cryoconite in Jakobshavn Isbrae, Greenland, and Canada Glacier, Antarctica. *Annals of Glaciology* **54**(63), 147–157.

Telling J and 9 others (2014) Spring thaw ionic pulses boost nutrient availability and microbial growth in entombed Antarctic Dry Valley cryoconite holes. *Frontiers in Microbiology* **5**, 694.

Terven J and Cordova-Esparza D (2023) A comprehensive review of YOLO: from YOLOv1 and beyond. arXiv 2023. *arXiv preprint arXiv*:2304.00501.

Tingey RJ (1991) Commentary on schematic geological map of Antarctica. Scale 1: 10 000 000. *Bulletin-Australia, Bureau of Mineral Resources, Geology and Geophysics* **238**, 1–30.

Tison J-L and 5 others (1998) Linking landfast sea ice variability to marine ice accretion at Hells Gate Ice Shelf, Ross Sea. *Antarctic Research Series* **74**, 375–407.

Traversa G, Fugazza D, Senese A and Diolaiuti GA (2019) Preliminary results on Antarctic albedo from remote sensing observations. *Geografia Fisica e Dinamica Quaternaria* **42**(2), 245–254. doi: 10.4461/GFDQ.2019.42.14

Traversa G, Zappetti M and Senese A (2021) Spring and summer spatial evolution of blue ice areas in Antarctica. *Geografia Fisica e Dinamica Quaternaria* **44**(1), 79–90. doi: 10.4461/GFDQ.2021.44.7

Webster-Brown JG, Hawes I, Jungblut AD, Wood SA and Christenson HK (2015) The effects of entombment on water chemistry and bacterial assemblages in closed cryoconite holes on Antarctic glaciers. *FEMS Microbiology Ecology* **91**(12), fiv144.

Weisleitner K, Perras A, Moissl-Eichinger C, Andersen DT and Sattler B (2019) Source environments of the microbiome in perennially ice-covered Lake Untersee, Antarctica. *Frontiers in Microbiology* **10**, 1019.

Weisleitner K and 5 others (2020) Cryoconite hole location in East-Antarctic Untersee Oasis shapes physical and biological diversity. *Frontiers in Microbiology* **11**, 1165.

Winther J-G, Jespersen MN and Liston GE (2001) Blue-ice areas in Antarctica derived from NOAA AVHRR satellite data. *Journal of Glaciology* **47**(157), 325–334. doi: 10.3189/172756501781832386

Zdanowski MK and 5 others (2017) Enrichment of cryoconite hole anaerobes: implications for the subglacial microbiome. *Microbial Ecology* **73**(3), 532–538. doi: 10.1007/s00248-016-0886-6

https://doi.org/10.1017/aog.2024.20 Published online by Cambridge University Press